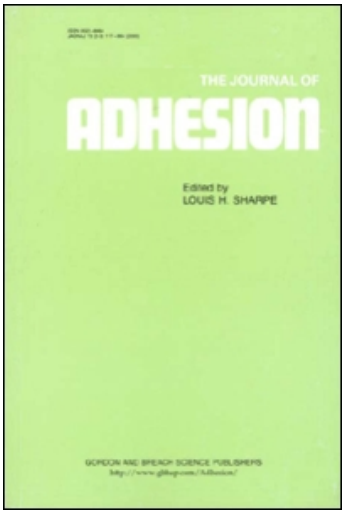

The Journal of Adhesion

Publication details, including instructions for authors and subscription information:
http://www.informaworld.com/smpp/title~content=t713453635

Aerosol Particle Deposition in a Recirculation Region

Amy Li[a]; Goodarz Ahmadi[a]; Michael A. Gaynes[b]; Raymond G. Bayer[b]
[a] Department of Mechanical and Aeronautical Engineering, Clarkson University, Potsdam, NY, USA [b] IBM Corporation, Endicott, NY, USA

To cite this Article Li, Amy , Ahmadi, Goodarz , Gaynes, Michael A. and Bayer, Raymond G.(1995) 'Aerosol Particle Deposition in a Recirculation Region', The Journal of Adhesion, 51: 1, 87 — 103
To link to this Article: DOI: 10.1080/00218469508009991
URL: http://dx.doi.org/10.1080/00218469508009991

J. Adhesion, 1995, Vol. 51, pp. 87–103
Reprints available directly from the publisher
Photocopying permitted by license only

Aerosol Particle Deposition in a Recirculation Region

AMY LI and GOODARZ AHMADI*

Department of Mechanical and Aeronautical Engineering, Clarkson University, Potsdam, NY 13699-5725, USA

and

MICHAEL A. GAYNES and RAYMOND G. BAYER

IBM Corporation, Endicott, NY 13760, USA

(Received March 3, 1994; in final form July 8, 1994)

Digital simulation results concerning aerosol particle transport and deposition in a recirculation region are presented. It is assumed that the particles are shed from sources near the back face of a block in a turbulent duct flow. The results show that a large number of particles may be captured by the block and the upper wall of the channel due to impaction and interception. The capture efficiencies increase as the source distance from the wall decreases. The gravitational effects on the particle deposition rate are also studied.

KEY WORDS aerosol; particle deposition; turbulent flow; recirculation zone; computational simulation; capture efficiency.

INTRODUCTION

Understanding the kinetics of aerosol dispersion and deposition has attracted considerable attention due to its significance in numerous industrial processes. Levich[1] provided an extensive review of particle diffusion in laminar flows. Cooper *et al.*[2] and Liu and Ahn[3] presented more recent studies in connection with microcontamination processes. Cooper[4] summarized the state of understanding of the microcontamination control in electronic industries. In turbulent flows, particles are transported by the mean motion and are dispersed by turbulence fluctuation and Brownian diffusion. Fuchs,[5] Davies,[6] Friedlander and Johnstone[7] and Clever and Yates[8] provided semi-empirical expressions for particle mass flux from a turbulent stream to smooth surfaces. Particle deposition on rough walls was studied by Browne[9] and Wood.[10] Extensive reviews on the subject were provided by Wood,[11] Hidy[12] and Papavergos and Hedley.[13]

* Corresponding author.

Using digital simulation to study diffusion of particles in turbulent pipe or channel flows was considered by a number of authors. Ahmadi and Goldschmidt[14] used digital simulation and analytical techniques to study the turbulent dispersion of small spherical particles. McLaughlin[15] and Ounis *et al.*[16] analyzed the aerosol particle deposition in a channel using a pseudospectral computer code to simulate the instantaneous turbulent flow field. Ounis and Ahmadi[17] also studied Brownian diffusion of submicron particles in the viscous sublayer. Abuzeid *et al.*[18] used a simple simulation technique to study the dispersion and deposition processes of suspended particles released from point sources in a turbulent channel flow. Recently, Li and Ahmadi[19-21] performed a series of digital simulations on deposition of aerosols of various sizes from point sources and initially uniform concon-centration in turbulent channel flows with smooth and rough surfaces. However, little work was done on particle transport and deposition in complex geometries of industrial interest. An example of this type of concern is the situation associated with the forced air cooling of electronic packages used in the computer industry. In these applications, air is forced through complex geometry passages which are a result of the overall packaging design and presence of individual components. Dust may then accumulate on and around various components and connectors, which can result in loss of cooling and electrical connector instabilities. Consequently, it is desirable to understand the effect of obstruction shapes on particle deposition rate.

Recently, Li *et al.*[22] developed a computational model for predicting dispersion and deposition of particles in ducts with complex geometries. The effects of air stream turbulence and its anisotropic nature were included in the model. The particle equation of motion used includes the Stokes drag, the Brownian, the Saffman lift, and the gravitational forces. The Brownian force was simulated as a white noise process. A thermodynamically-consistent, rate-dependent algebraic stress model was used to simulate the mean turbulent flow conditions. The instantaneous fluctuating turbulent velocity field was modeled by an anisotropic Gaussian random process.

In this study, the earlier developed computational model of Li *et al.*[22] was used to study the particle dispersion and deposition in the recirculation regions. Several digital simulations concerning particle migrations in a passage with an obstruction are performed. It is assumed that the particles are shed from sources near the back side of the block and initially have the same velocities as those of the fluid at the source location. The results show that a large number of particles may deposit on the block and the upper wall of the channel due to impaction and interception. The effect of direction of gravity on the deposition rate is also studied.

PARTICLE EQUATION OF MOTION

The equation of motion of a small aerosol particle is given by

$$\frac{du_i^p}{dt} = \frac{18\nu}{d^2 S C_c}(u_i - u_i^p) + \frac{2K\nu^{1/2} d_{ij}}{Sd(d_{lk}\, d_{kl})^{1/4}}(u_j - u_j^p) + \left(1 - \frac{1}{S}\right) g_i + n_i(t) \qquad (1)$$

and

$$\frac{dx_i}{dt} = u_i^p \tag{2}$$

where u_i^p is the velocity of the particle, x_i is its position, t is the time, d is the particle diameter, S is the ratio of particle density to fluid density, g_i is the acceleration of body force, $n_i(t)$ is the Brownian force per unit mass, ν is the the kinematic viscosity, $K = 2.594$ is the constant coefficient of Saffman's lift force, and u_i is the instantaneous fluid velocity with $u_i = \bar{u}_i + u_i'$, where $\bar{u}_i$ is the mean velocity of the fluid, and u_i' is the fluctuation component of fluid velocity. In equation (1), C_c is the Stokes-Cunningham slip correction given as

$$C_c = 1 + \frac{2\lambda}{d}(1.257 + 0.4\,e^{-1.1d/2\lambda}), \tag{3}$$

where λ is the molecular mean free path of the gas, and the deformation rate tensor d_{ij} is defined as

$$d_{ij} = \tfrac{1}{2}(u_{i,j} + u_{j,i}) \tag{4}$$

The first term on the right hand side of Equation (1) is the drag force due to the relative motion between particles and fluid. The second and third terms are the Saffman lift and the gravitational forces. The fourth term is the Brownian force. The drag force is always present and is generally a dominating force. The Saffman lift force becomes important for particles which are not too small in the regions with a strong shear field.

The Brownian force, which is very important for submicron particles, is modeled as a Gaussian white noise random process. The simulation procedure for the Brownian excitations was described at length by Li and Ahmadi[19,21] and Li *et al.*[22] and, hence, need not be repeated here.

FLOW SIMULATION

Equation (1) requires the knowledge of the instantaneous fluid velocity field. In this study, the STARPIC-RATE computational code[23] (a modified version of STARPIC computer developed by Lilley and Rhode[24]) was used and the mean turbulent flow condition in a duct with a rectangular obstructing block was evaluated. The computational model uses a nonlinear rate-dependent turbulence model. In these computations, it was assumed that the mean flow is steady and two-dimensional. A staggered grid with 96×48 node points was used. Uniform profiles for the mean velocities, turbulence kinetic energy and dissipation rate were specified at the duct inlet. Typically, values of inlet velocity $V = 5\,\text{m/s}$, inlet fluctuation energy $k = 0.25\,\text{m}^2/\text{s}^2$, $l = 0.4\,\text{mm}$, and $\varepsilon = k^{3/2}/l$, where l is the length (integral) scale, were

used. For the grids near the wall, the standard wall function boundary conditions were prescribed. At the outlet, zero normal gradient conditions were specified. The instantaneous turbulent fluctuating velocities are approximated as continuous anisotropic Gaussian random fields. A summary of the turbulence model used is provided in Appendix A. Additional details of the computational procedure were described at length by Li *et al.*[22] where comparisons of the model predictions for particle deposition rates with experimental data for the purpose of the code verification were also presented.

SIMULATION RESULTS

In this section, simulation results for dispersion and deposition of particles which are shed from point sources at different locations near the back side of the block are described. In addition, particle deposition from an initially uniform concentration in the back side of the block is also studied. Simulations are performed for a duct which is 2 cm wide and 10 cm long. A rectangular 1.25 cm × 0.61 cm block is assumed to be attached to the upper wall of the channel. This flow geometry resembles a segment of the cage passages of a computer. A temperature of 288°K, $\mu = 1.84 \times 10^{-5}$ N.s/m^2 and $\rho = 1.125$ kg/m^3 for air are used. For a mean air velocity of $V = 5.0$ m/s at the channel inlet, the flow Reynolds number based on the channel width is 6657, and the air is in a state of turbulent motion. A density ratio of particle to fluid $S = 2000$ and different particle diameters ranging from 0.01 μm to 50 μm are used in the analysis. It is assumed that when a particle touches a wall, the particle sticks to the surface.

Figure 1 shows the mean velocity vector plot, the turbulence fluctuation kinetic energy contour, and the root-mean-square (RMS) streamwise and vertical fluctuation velocity contours in the recirculation region. It is observed that a large recirculation region behind the block is formed. In addition, Figure 1a shows a smaller vortex in the corner along side of the block. Furthermore, the reattachment point on the upper wall is at $X \simeq 7.4$ cm and the center of the main vortex is at $X \simeq 5.8$ cm, $Y \simeq 1.7$ cm. The reattachment point on the block is at $Y \simeq 1.9$ cm. From Figures 1b–d, it is observed that the turbulence intensity is quite high in the recirculation region. Figures 1c and 1d also clearly show that the turbulence is highly anisotropic in the recirculation region with the RMS-streamwise fluctuation component being larger than the RMS-vertical component.

Figure 2 displays sample trajectories for 0.01 μm particles, which are shed from a point source near the back tip of the block (at $X_0 = 4.7$ cm, $Y_0 = 1.4$ cm). The gravitational effect is neglected in these simulations. Figure 2a shows a sample for which the particle is deposited on the upper wall of the channel. In Figure 2b the particle is entrapped in the recirculation region and eventually deposits on the block. Figure 2c shows a trajectory for which the particle escapes the recirculation region and leaves the channel.

Figure 3 shows sample particle trajectories for 1 μm and 10 μm particles which are shed from the same source location as in Figure 2. From Figure 3a, it is observed that one of the 1 μm particles is deposited on the upper wall, while the other one

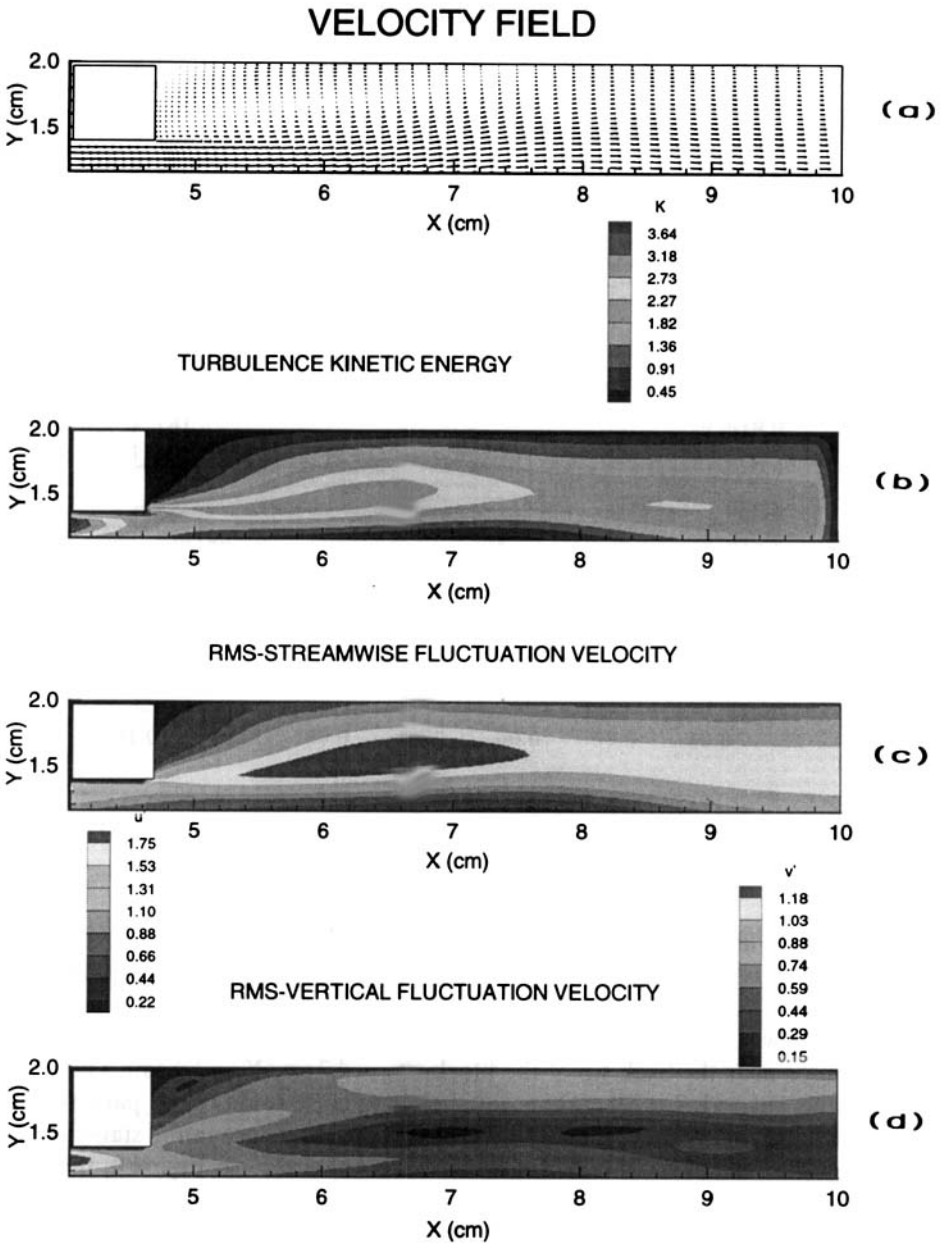

FIGURE 1 (a) mean flow field, (b) turbulent, fluctuation kinetic energy, (c) streamwise and, (d) vertical fluctuation components in the recirculation sone after a block.

leaves the channel. Figure 3b shows a sample trajectory of one of the 1 μm particles which is entrapped in the recirculation region and eventually deposits on the block. Three sample trajectories for 10 μm particles are shown in Figure 3c. It is observed that these particles may also deposit on the upper wall and/or the back side of the

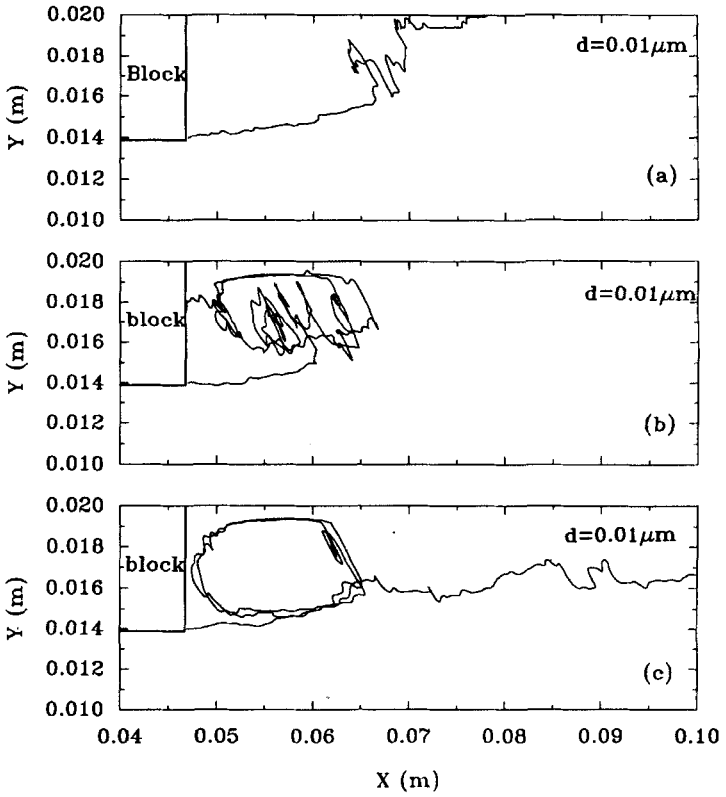

FIGURE 2 Sample trajectories for 0.01 μm particles for source location at $X_0 = 4.7$ cm, $Y_0 = 1.4$ cm.

block or could leave the channel. Comparing the sample trajectories shown in Figures 2 and 3, it is noticed that the 10 μm particles have the smoothest path due to their relatively larger inertia.

Figure 4 shows the particle trajectory statistics shortly after they are released from a point source near the back tip of the block ($X_0 = 4.7$ cm, $Y_0 = 1.4$ cm). The trajectory statistics beyond $X = 5.4$ cm are not shown because some of the particles may move backward and, therefore, may be counted more than once in the statistics. The trajectory statistics before $X = 4.7$ cm are not shown, either. In Figure 4, the mean particle paths are shown by solid lines, and σ denotes the particle trajectory standard deviation in the vertical direction. The absolute maximum and absolute minimum trajectories for an ensemble of 1000 particles are also shown in this Figure for reference. While these are sample dependent, they provide additional information on the amount of spreading of particles. It is observed that the spreading rates of different size particles are quite similiar. This implies that the turbulent diffusion is the dominant dispersion mechanism.

Several simulations were performed for various locations of the point source of particles within the recirculation region along side of the block. The results in terms

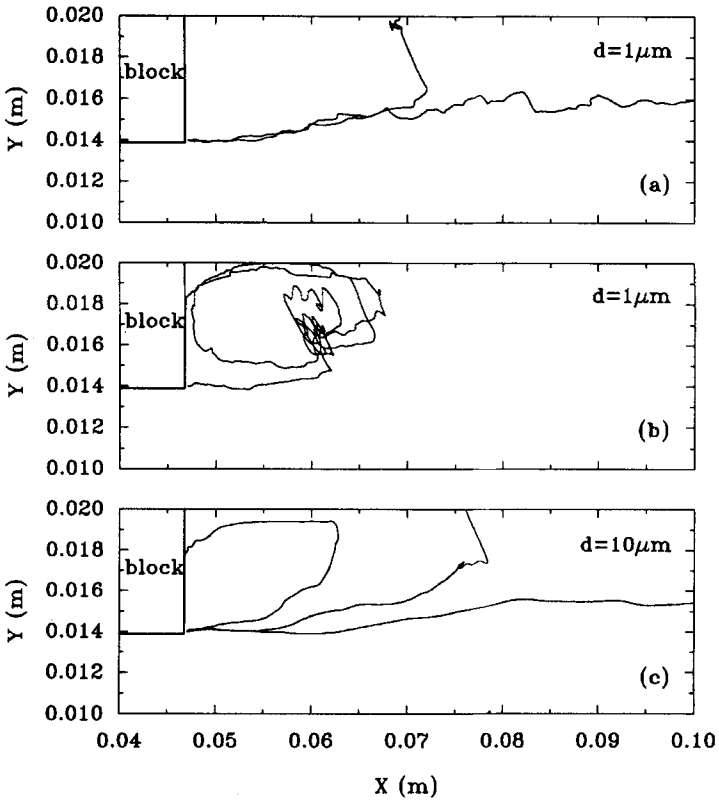

FIGURE 3 Sample trajectories for 1 and 10 μm particles for source location at $X_0 = 4.7$ cm, $Y_0 = 1.4$ cm.

of capture efficiency are shown in Figure 5. The capture efficiency is defined as

$$\eta = \frac{N_d}{N_H} \tag{5}$$

where N_d is the number of deposited particles and N_H is the number of particles swept by the block (1000 in these simulations). Here the capture efficiency becomes identical to the fraction of particles captured. Figure 5 shows that the capture efficiency of the block increases as the source becomes closer to the upper wall (Y_0 increases) for all sizes of particles. This is because, as the source distance from the wall decreases, particles are most easily entrained into the recirculation region. In particular, the deposition of 10 μm particles increases significantly as Y_0 increases. It should be emphasized that, for Y_0 larger than 1.7 cm, the flow field near the block has a significant velocity component towards the block which will further increase the deposition rate.

As observed from Figure 5, the capture efficiency of the upper wall decreases as Y_0 increases from 1.4 cm to 1.8 cm. This Figure also shows that the particles are more

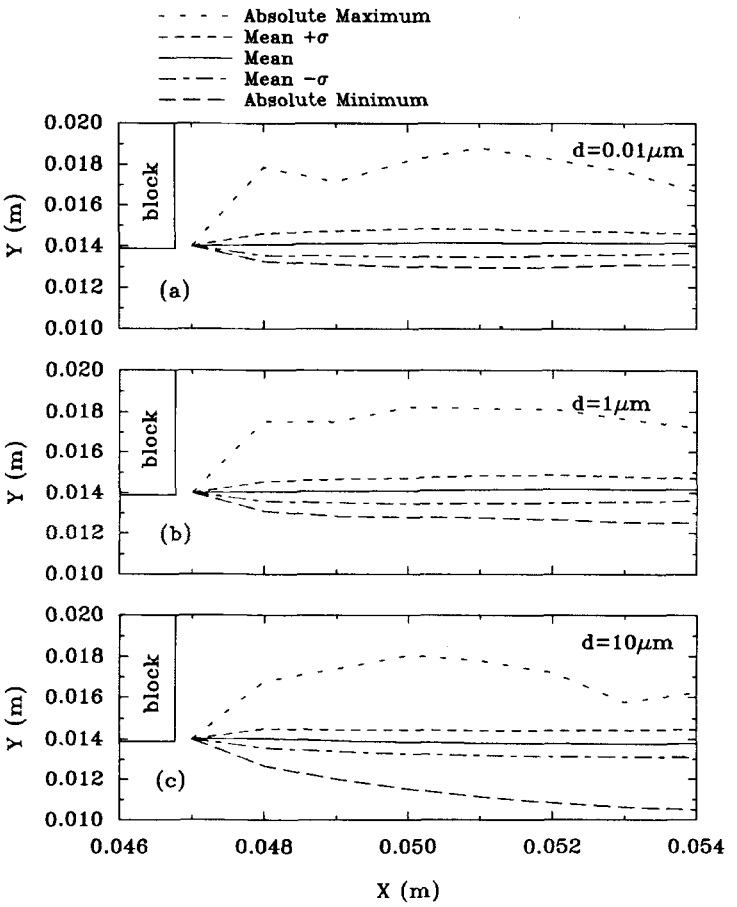

FIGURE 4 Particle trajectory statistics for a point source at $X_0 = 4.7\,\text{cm}$, $Y_0 = 1.4\,\text{cm}$ (a) $d = 0.01\,\mu\text{m}$, (b) $d = 1\,\mu\text{m}$, (c) $d = 10\,\mu\text{m}$.

likely to be deposited on the back face of the block than on the upper wall. The exception is the 10 μm particles and the source distance $Y_0 \simeq 1.4\,\text{cm}$ for which the depositions are comparable.

The variations of fraction of particles that leave the channel with source location are shown in Figure 6. It is observed that, as the source becomes closer to the upper wall (Y_0 increases), the fraction of particles that leave the channel decreases. Although trends of variation shown in Figures 5 and 6 are very similar for different sized particles, the magnitudes are dramatically different. For example, the number of 10 μm particles that leave the channel is significantly higher than those of 0.01 μm and 1 μm particles. The numbers of 0.01 μm and 1 μm particles that are deposited on the upper wall are more than twice as many as of that of 10 μm particles. The numbers of 0.01 μm and 1 μm particles that are deposited on the block are, however, much higher when compared with that of the 10 μm particles.

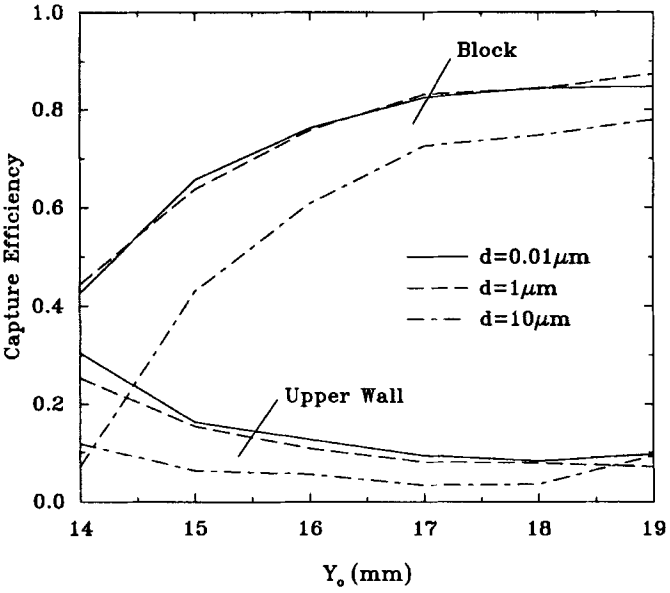

FIGURE 5 Variations of capture efficiency with point source location Y_0.

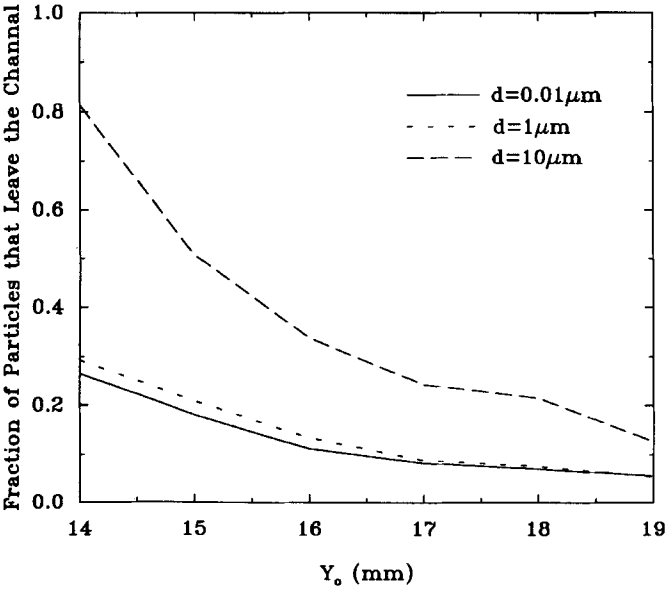

FIGURE 6 Variations of fraction of particles that leave the channel with point source location Y_0.

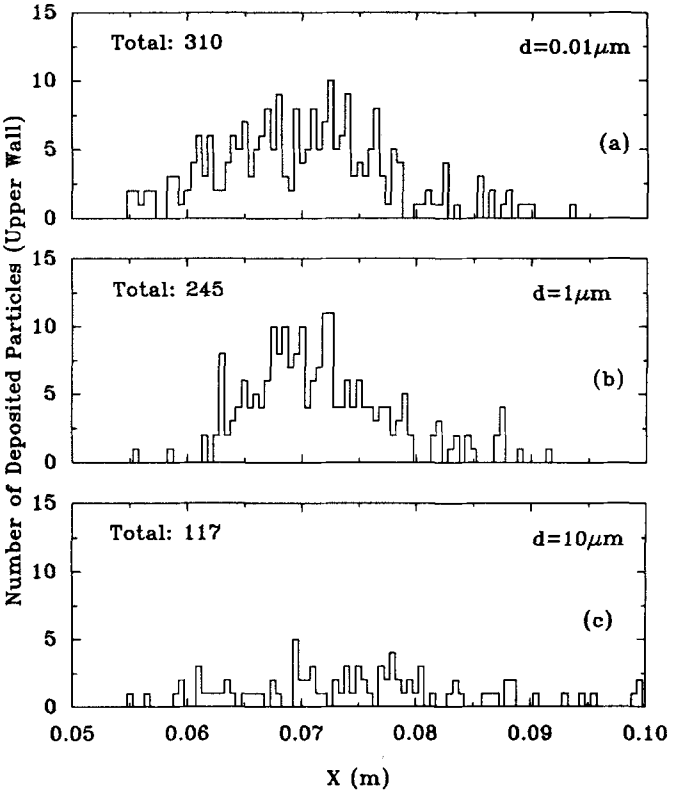

FIGURE 7 Distributions of deposited particles on the upper wall for particles which are shed uniformly from the block, (a) $d = 0.01$ μm, (b) $d = 1$ μm, (c) $d = 10$ μm.

To provide an understanding of the deposition rate of particles which are shed uniformly from the back face of the block, a series of simulations are also performed. Two thousand particles are released with Y_0 randomly distributed between 1.4 and 2 cm and $X_0 = 4.7$ cm (about 0.3 mm away from the block). Thus, the initial concentration in this region is uniform. Simulations are performed for a duration of 9 seconds (9000 time steps). The distributions of the deposited 0.01 μm, 1 μm and 10 μm particles on the upper wall are shown in Figure 7. The amplitudes shown in this figure correspond to the total number of deposited particles on the surface. It is observed that three hundred and ten 0.01 μm and two hundred and forty five 1 μm particles are deposited on the upper wall of the channel, while only one hundred and seventeen 10 μm particles are deposited on the same surface. Most of 0.01 μm and 1 μm particles are deposited in the distance range of $6 < X < 8$ cm near the reattachment point. As noted before, particles smaller than 1 μm generally follow the stream lines and are projected toward the wall. The 10 μm particles, however, follow their initial straight trajectories and deviate from the flow streamlines due to their relatively large inertia. Most 10 μm particles, therefore, follow their initial straight trajectories and leave the channel. It should also be pointed out that 80, 31 and 85

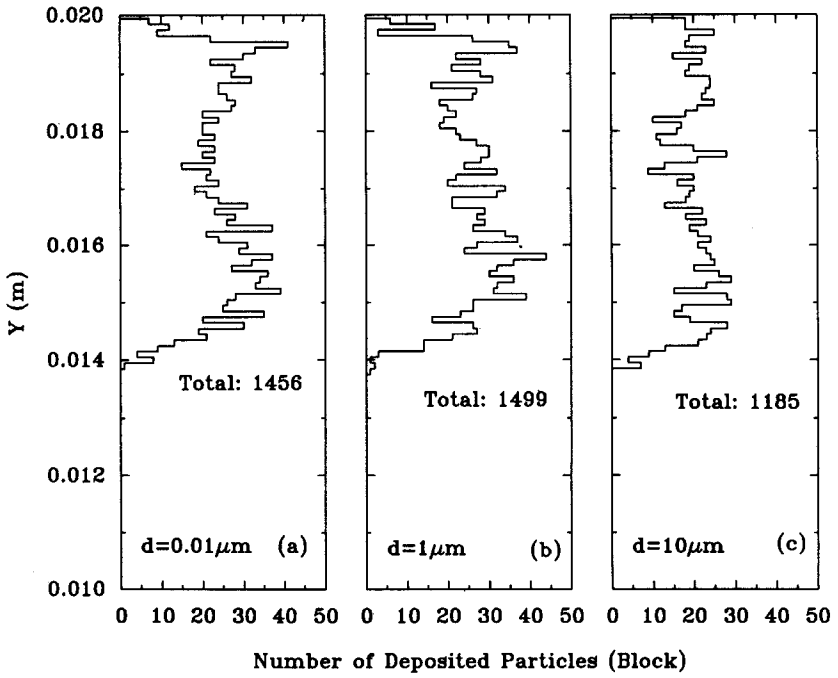

FIGURE 8 Distributions of deposited particles on the block for particles which are shed uniformly from the block. (a) $d = 0.01\ \mu m$, (b) $d = 1\ \mu m$, (c) $d = 10\ \mu m$.

particles with diameters of 0.01 μm 1 μm and 10 μm, respectively, deposit on the upper wall very near the block which are not shown in Figure 7. This high rate of deposition is due to the presence of the small clockwise vortex in the corner along side of the block which moves the particles toward the wall.

The distributions of the deposited particles on the block are shown in Figure 8. It is observed that about fifteen hundred 0.01 μm and 1 μm particles are deposited on the backface of the block, while about twelve hundred 10 μm particles have reached the surface of the block. The deposited particle distributions on the block are roughly uniform.

Figure 9 shows the distribution of particles at the outlet of the channel. It is observed that two hundred and twenty nine 0.01 μm, two hundred and forty four 1 μm, and six hundred and thirty-seven 10 μm particles leave the channel. As mentioned before, over the first few time steps, all particles roughly follow the local flow streamlines. However, as the streamlines bend due to the presence of the recirculation zone, very small particles, which follow the streamline, fall into the recirculation zone due to their Brownian motion and turbulence fluctuations. As a result, more of the smaller particles are captured by the recirculating flow and are deposited on the upper wall of the channel and/or on the backside of the block.

The particle concentration profiles at the channel exit shown in Figure 9 have large spreads roughly spanning the entire distance between the source location and the channel wall. There are also sharp peaks near the wall. These peaks appear to be

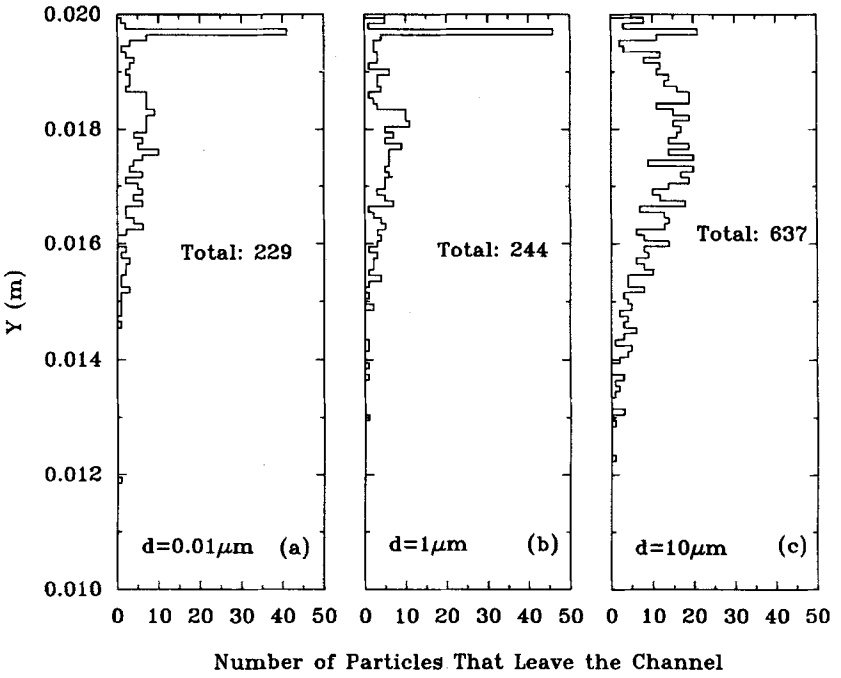

FIGURE 9 Particle concentration at the outlet of the channel for particles which are shed uniformly from the block. (a) $d = 0.01\,\mu m$, (b) $d = 1\,\mu m$, (c) $d = 10\,\mu m$.

due to turbophoresis phenomena as described by Reeks.[25] Accordingly, particles with higher velocity fluctuations perpendicular to the wall are transported into the region with lower fluctuation velocities closer to the wall. At distances very close to the wall the turbulent fluctuation velocity becomes negligibly small and, therefore, the particle dispersion mechanism becomes ineffective. That, in turn leads to an increase in concentration of particles in the neighbourhood of the wall.

Variations of capture efficiencies of the back surface of the block, the upper wall of the channel, and the combined surfaces with the Stokes number are shown in Figure 10. The corresponding particle diameters for the present flow conditions are also shown in this figure for reference. Here, the Stokes number is defined as the ratio of the stopping distance of a particle to the block height H, *i.e.*,

$$Stk = \frac{\tau V}{H} \tag{6}$$

It is observed that the capture efficiency of the block is much larger than the upper wall. This is because the particles which are released from sources at $Y_0 > 16\,mm$ are mostly deposited on the block. The capture efficiencies change only slightly as Stk increases from 10^{-5} to 0.01. As Stk increases beyond 0.01, the capture efficiency of the block decreases, while that of the upper wall increases. It is also observed from this figure that the fraction of particles that leave the channel generally increases as

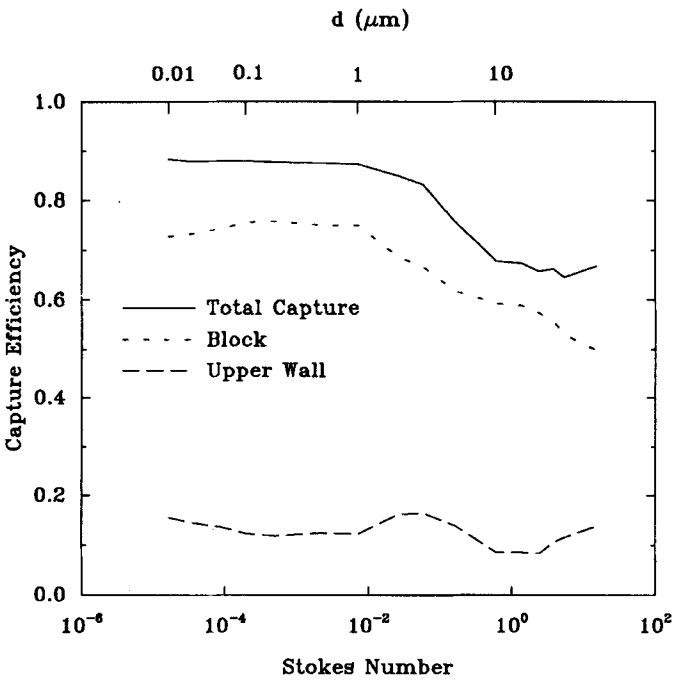

FIGURE 10 Variations of capture efficiency of particles which are shed uniformly from the block with the Stokes number.

Stk increases. The simulation results show that about one third of 10 μm particles leave the channel due to their inertia.

A number of simulations are performed and the gravitational sedimentation effect on particle deposition rate in the recirculation region is studied and the results are shown in Figure 11. The gravity is assumed to be directed upward (toward the upper wall), downward (toward the lower wall), toward the back face of the block, and toward the channel exit. These cover the cases that the block is on the upper wall or on the bottom wall in a horizontal channel, and/or on the side walls of a vertical duct. The simulation results in the absence of gravitation effects are also shown in this figure for comparison. Since the effect of gravity on particles smaller than 1 μm particles is negligible, the results for larger particles only are shown in Figure 11.

This figure shows that the direction of gravity affects the particle deposition rate. In particular, when the gravity is directed away from the block, the capture efficiency of the block is reduced. For the gravity direction being toward the block, the capture efficiency of the block increases. However, the recirculating flow pattern and turbulence seem to dominate the particle deposition rate and the effect of gravity is not as significant.

The gravity also affects the capture efficiency of the upper wall. The capture efficiency of the upper wall decreases when the gravity is directed away from the upper wall and increases when the gravity is directed toward the upper wall.

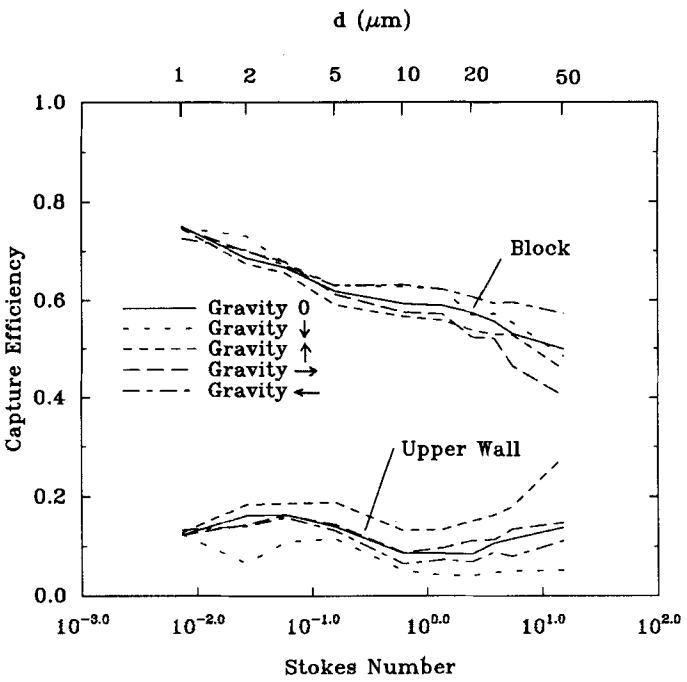

FIGURE 11 Variations of capture efficiency of particles with the Stokes number including the gravitational effects.

However, the direction of gravity does not have a significant efffect on the capture efficiency of the upper wall. The recirculating flow conditions overwhelm the gravitational effects when the gravity is away from the wall. The gravitational effects become significant only at distances very near the wall where the turbulence fluctuations become small. In this case, the gravity could prevent the particles from being deposited and, thus, allow the particles to be re-entrained into the recirculation region. For 50 μm particles, Figure 11 shows that the gravitational sedimentation effects are significant and affect the particle deposition rate.

CONCLUSIONS

In this work, simulation results for deposition of aerosol particles in a recirculation region is described. A thermodynamically-consistent, rate-dependent algebraic stress model is used to simulate the mean turbulent field. The instantaneous turbulence fluctuation is simulated as a continuous nonisotropic Gaussian random field. The Brownian motion is modeled as a white noise process. The particle equation of motion used includes the Brownian force, the Saffman lift force, and turbulent dispersion effects. Several digital simulations concerning the dispersion and

deposition of aerosol particles are performed. Based on the presented results, the following conclusions may be drawn:

- Large fractions of particles which are shed from the block into the recirculation flow region deposit on the block or the channel wall.
- Impaction is the dominant mechanism for particle deposition in the recirculating region.
- Turbulent dispersion is the dominating mechanism for particle spreading when compared with the Brownian motion.
- As the distance of source location from the wall decreases, the capture efficiencies increases.
- For uniform particle shedding from the back face of the block, the capture efficiency varies slightly for $10^{-5} < Stk < 0.01$. The capture efficiency of the block decreases and that of the upper wall increase as Stk increases beyond 0.01.
- The direction of gravity affects the capture efficiency but not to a significant extent.

Acknowledgements

Various stages of this work were supported by the International Business Machines Corporation (IBM-Endicott), the New York State Science and Technology Foundation through the Center for Advanced Material Processing (CAMP) of Clarkson University, and the US Department of Energy (University Coal Research Program, PETC), under Grant DE-FG22-94 PC 94213.

References

1. V. G. Levich, *Physiochemical Hyrdrodynamics* (Prentice-Hall, Englewood Cliffs, NJ, 1972).
2. D. W. Cooper, M. H. Peters, and R. J. Miller, *Aerosol Sci. Technol.* **11**, 133–143 (1989).
3. B. Y. H. Liu, and K. H. Ahn, *Aerosol Sci. Technol.* **6**, 215–224 (1987).
4. D. W. Cooper, *Aerosol Sci. Technol.* **5**, 287–299 (1986).
5. N. A. Fuchs, *The Mechanics of Aerosols*, (Pergamon, Oxford, 1964).
6. C. N. Davies, *Aerosol Science* (Academic Press, London, 1966).
7. S. K. Friedlander, and H. H. Johnstone, *Ind. Eng. Chem.* **49**, 1151–1156 (1957).
8. J. W. Cleaver and B. Yates, *Chemical Eng. Sci*, **30**, 983–992 (1975).
9. L. W. B. Browne, *Atmospheric Environment* **8**, 801–816 (1974).
10. N. B. Wood, *J. Aerosol Sci.* **12**, 275–290 (1981).
11. N. B. Wood, *Institute of Energy* **76**, 76–93 (1981).
12. G. M. Hidy, *Aerosols, An Industrial and Environmental Science* (Academic Press, New York, 1984).
13. P. G. Papavergos, and A. B. Hedley, *Chem. Eng. Des.* **62**, 275–295 (1984).
14. G. Ahmadi, and V. W.Goldschmidt, Technical Report FMTR–70–3, Purdue University (1970). Also *J. Appl. Mech. ASME* **38**, 561–563 (1971).
15. J. B. McLaughlin, *Phys. Fluids, A* **1**, 1211–1224 (1989).
16. H. Ounis, G. Ahmadi, and J. B. McLaughlin, *J. Colloid and Interface. Sci.* **143**, 266–277 (1991).
17. H. Ounis and G. Ahmadi, *ASCE J. Engng. Mech.* **115**, 2107–2121 (1989).
18. S. Abuzeid, A. A Busnaina, and G. Ahmadi, *J. Aerosol Sci.* **22**, 43–62 (1991).
19. A. Li, and G. Ahmadi, *Aerosol. Sci. Technol.* **16**, 209–226 (1992).
20. A. Li, and G. Ahmadi, *Aerosol. Sci. Technol.* **18**, 11–24 (1993).
21. A. Li, and G. Ahmadi, *Int. J. Engng. Sci.* **31**, 435–451 (1993).
22. A. Li, and G. Ahmadi, R. G. Bayer, and M. A. Gaynes, *J. Aerosol. Sci.* **25**, 91–112 (1994).
23. S. J. Chowdhury and G. Ahmadi, *Int. J. Non-linear Mechanics* **27**, 705–718 (1992).
24. D. G. Lilley, and D. L. Rhode, NASA Contractor Report 3442 (1982).
25. M. W. Reeks, *J. Aerosol Sci.* **14**, 729–739 (1983).

APPENDIX A

Turbulent Model

For an incompressible fluid, the equations of continuity and balance of momentum for the mean motion are given by Chowdhury and Ahmadi[23] as

$$\frac{\partial \bar{u}_i}{\partial x_i} = 0 \tag{7}$$

$$\frac{\partial \bar{u}_i}{\partial t} + \bar{u}_j \frac{\partial \bar{u}_i}{\partial x_j} = -\frac{1}{\rho}\frac{\partial \bar{p}}{\partial x_i} + \nu \frac{\partial^2 \bar{u}_i}{\partial x_j \partial x_j} - \frac{\partial}{\partial x_j} R_{ij} \tag{8}$$

where $\bar{p}$ is the mean pressure, ρ is the constant mass density, and R_{ij} is the Reynolds stress tensor (second moment of fluctuation velocity). The thermodynamically-consistent anisotropic expression for the Reynolds stress tensor is given as

$$R_{ij} = \frac{2}{3}k\delta_{ij} - 2\nu^T \bar{d}_{ij} - \nu^T \frac{k}{\varepsilon}\left[\alpha \frac{\hat{D}}{Dt}\bar{d}_{ij} + \gamma \frac{k}{\varepsilon}\bar{d}_{lk}\bar{d}_{kl}\bar{d}_{ij} - \beta\left(\bar{d}_{ik}\bar{d}_{jk} - \frac{1}{3}\bar{d}_{kl}\bar{d}_{kl}\delta_{ij}\right)\right] \tag{9}$$

where k is the turbulence kinetic energy, ν^T the turbulent eddy viscosity, ε is the energy dissipation rate and α, β and γ are certain constants. Here,

$$\frac{\hat{D}}{Dt}\bar{d}_{ij} = \frac{\partial}{\partial t}\bar{d}_{ij} + \bar{u}_k \frac{\partial \bar{d}_{ij}}{\partial x_k} + \bar{d}_{ik}\bar{\omega}_{kj} + \bar{d}_{jk}\bar{\omega}_{ki} \tag{10}$$

is the co-rotational (Jaumann) derivative of the mean deformation rate tensor, and the deformation rate tensor and spin tensors are, respectively, defined as

$$\bar{d}_{ij} = \frac{1}{2}\left(\frac{\partial \bar{u}_i}{\partial x_j} + \frac{\partial \bar{u}_j}{\partial x_i}\right), \quad \bar{\omega}_{jk} = \frac{1}{2}\left(\frac{\partial \bar{u}_j}{\partial x_k} - \frac{\partial \bar{u}_k}{\partial x_j}\right) \tag{11}$$

The eddy viscosity ν^T is given by

$$\nu^T = C^\mu k^2/\varepsilon, \tag{12}$$

where C^μ is a constant. Note that R_{11} and R_{22}, respectively, are the mean-square streamwise and vertical fluctuation velocity.

The equations governing the kinetic energy of turbulence and the dissipation rate are

$$\frac{\partial k}{\partial t} + \bar{u}_j \frac{\partial k}{\partial x_j} = \frac{\partial}{\partial x_j}\left[\left(\nu + \frac{\nu^T}{\sigma^k}\right)\frac{\partial k}{\partial x_j}\right] - R_{ij}\frac{\partial \bar{u}_i}{\partial x_j} - \varepsilon, \tag{13}$$

$$\frac{\partial \varepsilon}{\partial t} + \bar{u}_j \frac{\partial \varepsilon}{\partial x_j} = \frac{\partial}{\partial x_j}\left[\left(\nu + \frac{\nu^T}{\sigma^\varepsilon}\right)\frac{\partial \varepsilon}{\partial x_j}\right] - C^{\varepsilon 1}\frac{\varepsilon}{k}R_{ij}\frac{\partial \bar{u}_i}{\partial x_j} - C^{\varepsilon 2}\frac{\varepsilon^2}{k} \tag{14}$$

The values of constants are given as

$$C^{\mu} = 0.09, \quad \sigma^{k} = 1, \qquad \sigma^{\varepsilon} = 1.3, \; C^{\varepsilon 1} = 1.44, \quad C^{\varepsilon 2} = 1.92, \tag{15}$$

$$\alpha = 0.93, \quad \beta = 0.54, \quad \gamma = \frac{\beta^2}{48} = 0.006. \tag{16}$$

This thermodynamically-consistent model leads to an anisotropic effective viscosity and is capable of predicting the expected turbulence normal stress differences. Chowdhury and Ahmadi[23] have shown that the present model predictions are in reasonable agreement with the experimental data for a number of separated and non-separated, as well as swirling and non-swirling flows.